AGU ADVANCING EARTH AND SPACE SCIENCES

JAMES Journal of Advances in Modeling Earth Systems®

RESEARCH ARTICLE
10.1029/2024MS004689

Key Points:

- VarDyn is a method using reduced physical models and a variational scheme to map sea surface height (SSH) and sea surface temperature (SST) from altimetric and microwave satellite data
- Tested against recent high-resolution data, VarDyn improves the accuracy of SSH and SST maps compared to operational products
- SSH mapping especially benefits from SST for a two altimeters configuration, opening the way of refining climate SSH records

Correspondence to:
F. Le Guillou,
florian.leguillou@esa.int

Citation:
Le Guillou, F., Chapron, B., & Rio, M.-H. (2025). VarDyn: Dynamical joint-reconstructions of sea surface height and temperature from multi-sensor satellite observations. *Journal of Advances in Modeling Earth Systems*, *17*, e2024MS004689. https://doi.org/10.1029/2024MS004689

Received 3 SEP 2024
Accepted 11 MAR 2025

Author Contributions:
Conceptualization: Marie-Helene Rio
Formal analysis: Bertrand Chapron
Supervision: Marie-Helene Rio
Writing – review & editing: Bertrand Chapron, Marie-Helene Rio

VarDyn: Dynamical Joint-Reconstructions of Sea Surface Height and Temperature From Multi-Sensor Satellite Observations

Florian Le Guillou[1], Bertrand Chapron[2,3], and Marie-Helene Rio[1]

[1]European Space Research Institute (ESA-ESRIN), Frascati, Italy, [2]Ifremer, CNRS, IRD, LOPS, University of Brest, Plouzané, France, [3]Ifremer, INRIA, ODYSSEY, Plouzané, France

Abstract The VarDyn hybrid methodology, which combines minimal physically based constraints with a variational scheme, is demonstrated to enhance the mapping of sea surface height (SSH) and sea surface temperature (SST). By synthesizing multi-modal satellite observations, VarDyn produces SSH and SST maps with improved accuracy compared to operational products, achieving reductions in Root Mean Square Error and enhancements in effective spatial resolution. While most improvements are observed in highly energetic ocean regions, SSH map accuracy also improves slightly in low-energy regions—a significant advancement over other methods. VarDyn SSH fields and the associated geostrophic velocities show strong agreement with newly available high-resolution instantaneous SWOT estimates. Notably, the assimilation of SST proves particularly beneficial for SSH reconstruction when only two altimeters are available. The VarDyn methodology potentially offers a robust framework for refining climate SSH records by jointly assimilating SSH data from two altimeters and SST data from microwave sensors.

Plain Language Summary By combining fundamental physical principles with advanced data processing techniques, the joint reconstruction of sea surface height (SSH) and sea surface temperature (SST) is demonstrated. Using satellite data, this approach systematically produces more accurate SSH and SST maps, with particularly noticeable improvements in highly dynamic ocean regions. Additionally, the method significantly enhances mapping performance in calmer ocean areas. The results align closely with new high-resolution satellite observations. Notably, when only two altimeter satellites are available, incorporating SST data significantly improves SSH mapping capabilities. This methodology offers a promising tool for refining climate records by consistently integrating previously available medium-resolution SST and altimeter measurements.

1. Introduction

Satellite altimetry has revolutionized our view of upper ocean dynamics. Global precise measurements of sea surface height (SSH), alone, in combination with other space-borne or in situ data, are now systematically used to identify, characterize and track mesoscale eddies (Frenger et al., 2015; Liu et al., 2023; Vazquez-Cuervo et al., 1996), diagnose ocean heat transport (Chen & Yu, 2024; Siegelman & Klein, 2020), inform about ocean circulation at the surface (Ciani et al., 2019; Kugusheva et al., 2024; Rio & Santoleri, 2018) and at depth (Wang et al., 2013), understand the dynamical coupling between the atmosphere and the ocean (Combot et al., 2024; Oliver et al., 2017; Trott et al., 2021).

These SSH satellite observations are irregularly distributed in space and time. Many scientific and operational applications, that is, the reconstruction of global geostrophic currents, then rely on interpolation techniques to provide gap-free regularly-sampled SSH maps, combining several nadir-looking altimeters (Le Traon et al., 1998). This is the case of the most commonly used SSH maps, the Developing Use of Altimetry for Climate Studies (DUACS) products. Still, large gaps between altimeter tracks, reaching about 200 km in the zonal direction at the equator, and intrinsic limitations of linear interpolation schemes prevent the reconstruction of small-scale and/or non-linear structures. Ballarotta et al. (2019) quantify the space/time effective resolutions of the SSH interpolated products, reporting, at mid-latitude, resolutions of 150 km in space and 10 days in time. In such a context, the new Surface Water Ocean Topography (SWOT) mission now provides instantaneous SSH observations of small-scale structures, down to 10–30 km in space. Yet, its long revisit time of 21 days still complicates the reconstruction of their trajectories in both space and time.

More innovative mapping algorithms have then been proposed, implemented, and compared to circumvent these space/time resolution limitations. Some of these techniques rely on multi-scale and multivariate approaches (Ballarotta et al., 2023), others on deep learning and variational techniques (Beauchamp et al., 2023), and also on analog forecasting and Kalman filters (Zhen et al., 2020). Hybrid methods can help combine physics with statistical methods. For instance, several studies used a 1.5-layer Quasi-Geostrophic (QG) model to dynamically interpolate the SSH observations (Ballarotta et al., 2020; Le Guillou et al., 2023). These hybrid methodologies generally demonstrate significant gains for the effective resolutions of the SSH maps. Still, small-scale (less than 100 km) processes are generally filtered out.

Complementary to altimeter SSH measurements, instantaneous ocean surface observations from space using radar, microwave imagers, and optical instruments, at synoptic scale O(100 km) and resolution O(100 m), often reveal a mixture of rich oceanic signatures, for example, filaments, upwelling and spiraling eddies, etc. Satellite images of surface tracers, for example, sea surface temperature (SST), often capture subtle variations related to the underlying complex small-scale turbulent dynamical flows (e.g., Abraham & Bowen, 2002). Oceanic fronts commonly sharpen to scales much less than 1 km and can develop intense current gradients. However, while tracer images can be used to obtain information about the location and geometry of ocean structures, it is difficult to directly quantify dynamical properties from these instantaneous snapshots (Turiel et al., 2005).

Several methods explicitly aimed to identify spatio-temporal dependencies between SST data and upper ocean circulation. Using image pairs, estimates of the surface velocities can be performed by following small-scale features (Emery et al., 1986; Flament et al., 1985; Vigan et al., 2000). After Kelly (1989) or Ostrovskii and Piterbarg (1995), advection-diffusion equations have also been proposed to interpret the evolution of SST anomalies (Ba et al., 2012; Ciani et al., 2019; Rio & Santoleri, 2018; Rio et al., 2016). Others rely on dynamical rationales using the Surface Quasi-Geostrophic (SQG) theory (González-Haro & Isern-Fontanet, 2014; Isern-Fontanet et al., 2006, 2014; LaCasce & Mahadevan, 2006; Lapeyre & Klein, 2006). More recently, deep learning algorithms further emerged, using various architectures, to extract high-resolution SST information to improve the SSH reconstruction (Archambault et al., 2022; Buongiorno Nardelli et al., 2022; Fablet et al., 2023, 2024; Martin et al., 2023). Finally, tracer Lagrangian advection using SSH-derived geostrophic surface currents can also be used. Lagrangian advection can build fine-scale surface fronts and filaments (Dencausse et al., 2013; Rogé et al., 2015), to help refine upper ocean velocities to match locations of intense tracer gradient (Gaultier et al., 2013), and/or to evaluate extended Okubo-Weiss criterion (Berti & Lapeyre, 2014; Mezić et al., 2010; Resseguier et al., 2022).

In the present study, the strategy is also to dynamically combine SSH and SST satellite observations. The general idea is to extend the SSH mapping methodology presented by Le Guillou et al. (2023), the so-called BFN-QG, which uses a QG-based dynamical framework in an inversion technique called Back and Forth Nudging. Here, a dynamical constraint is added to reconstruct the SST field, and the inversion method is now based on a 4D variational scheme. The dynamical constraint on SST follows an advection-diffusion equation. Coupling with SSH is ensured by assuming an SST Lagrangian advection using the SSH-derived geostrophic current velocities.

This proposed mapping technique, called VarDyn, is tested and compared to real nadir-looking SSH measurements and 2D microwave SST data over a region spanning the extended Gulf Stream region. For this region, the QG theory is expected to provide a good description of ocean dynamics in the mesoscale range. In this range, rotation and stratification are still quite important, but the Rossby number is sufficiently small. Opportunely, reconstructed SSH fields can now further benefit comparisons with newly available independent SWOT high-resolution data. SST-reconstructed fields are more classically compared to infrared high-resolution satellite sensor measurements. Mapping performances are also compared with operational products, that is, DUACS for SSH and REMSS for SST. Special attention is performed to evaluate the impact of SST observations to improve SSH reconstructions under different altimeter constellations.

The paper is organized as follows. In Section 2, the SSH/SST synergies are illustrated from satellite observations, and the data is presented as input and for validation purposes. The VarDyn methodology is described in Section 3 and performances are discussed in Section 4. Concluding remarks are given Section 5.

2. Data and Study Area

2.1. Input Data Sets

Near-real-time along-track SSH products are considered. The 1 Hz product of all available missions (Sentinel-6A, Jason-3, Sentinel-3A, Sentinel-3B, Saral/AltiKa, Cryosat-2, HY-2B) are used. DUACS multimission altimeter data processing system ensures all the mission measurements are homogenized to Sentinel-6A ones (reference missions).

For SST observations, estimates from the Advanced Microwave Scanning Radiometer (AMSR-2) and the Global Precipitation Measurement Microwave Imager (GMI) are considered. To benefit from their time sampling coverage, both ascending and descending passes are selected. Diurnal cycle corrections are not applied.

SST from IR sensors do not enter the reconstruction scheme: (a) small-scale structures possibly detected with IR sensors are generally smoothed out with medium-resolution microwave data, and not always correlated with small-scale SSH features (see Section 2.3); (b) IR data are affected by clouds, Figure 1, making it difficult to apply the heat conservation principle. The latter may affect the performance of the reconstruction method; see Sections 3.1 and 3.2.

2.2. Validation Data Sets

For SSH, the validation benefits data from the recently launched SWOT mission. It provides unprecedented high-resolution SSH measurement over a 120 km wide swath. The Level-3 Science product at 2 km resolution is used. The processing methodology for SWOT Level 3 products, as detailed in Dibarboure et al. (2024), involves several sequential steps. These include Level-2 geophysical corrections, editing (e.g., detection and removal of spurious measurements), and multi-mission calibration. Besides, to minimize the impact of observational noise during performance evaluation, we used the denoised SSH variable processed with a U-Net neural network-based noise mitigation algorithm (Tréboutte et al., 2023).

For SST, IR data from polar and geostationary satellites are used. We use the multi-sensor Polar InfraRed (PIR) and Geostationary InfraRed (GIR) Level-3 data sets, daily interpolated, over a 1/10° regular grid.

Performances of the reconstructed field are also compared to operational products, also processed with similar input data sets (see Section 2.1): (a) for SSH, the DUACS gridded Level-4 product; (b) for SST, the Microwave gridded Level-4 products from the Remote Sensing Systems (REMSS). These two products provide global, daily maps over a 1/4° regular grid.

2.3. Study Area

The study region spans the extended Gulf Stream region (80°–10°W, 25°–50°N), Figure 1. This region offers various energetic regimes, a great playground to test various SSH reconstruction methods (Beauchamp et al., 2023; Fablet et al., 2024; Le Guillou et al., 2021; Martin et al., 2023). High SST gradients occur, crucial for the reconstruction of ocean surface dynamics from SST (Rio & Santoleri, 2018).

The time period of interest covers August 2023 to May 2024 to benefit from high-resolution SWOT data (see Section 2.2), providing a unique instantaneous 2D SSH view, with a 120km-wide swath, Figure 1. It represents an invaluable source of observations to compare with reconstructed SSH fields.

Over this region, SSH and SST fields are generally correlated. The degree of correlation varies according to seasons, oceanic features, and spatial scales. Illustrated in Figure 1, the SWOT-derived 2D SSH structures align relatively well with SST structures captured by microwave and infrared sensors. A 0.15 m level-set SSH superimposed on the SST images, in Figure 1, clearly matches an SST isoline. Such an alignment between the two fields is often anticipated. Over areas where mixed layer instability is active, surface geostrophic velocities may indeed be largely related to surface buoyancy anomalies (Isern-Fontanet et al., 2006; Lapeyre, 2009). Alignments between SSH and SST fields are then intensified in winter. In summer, warming heat fluxes may substantially reduce SST gradients to lower correlation (Le Goff et al., 2016). Cold SST anomalies are still more favorably correlated with low SSH anomalies, for example, the mesoscale eddy in Figure 1. Note that under an SQG framework, SSH-related stream function may be expressed from a low-pass filtered high-resolution SST.

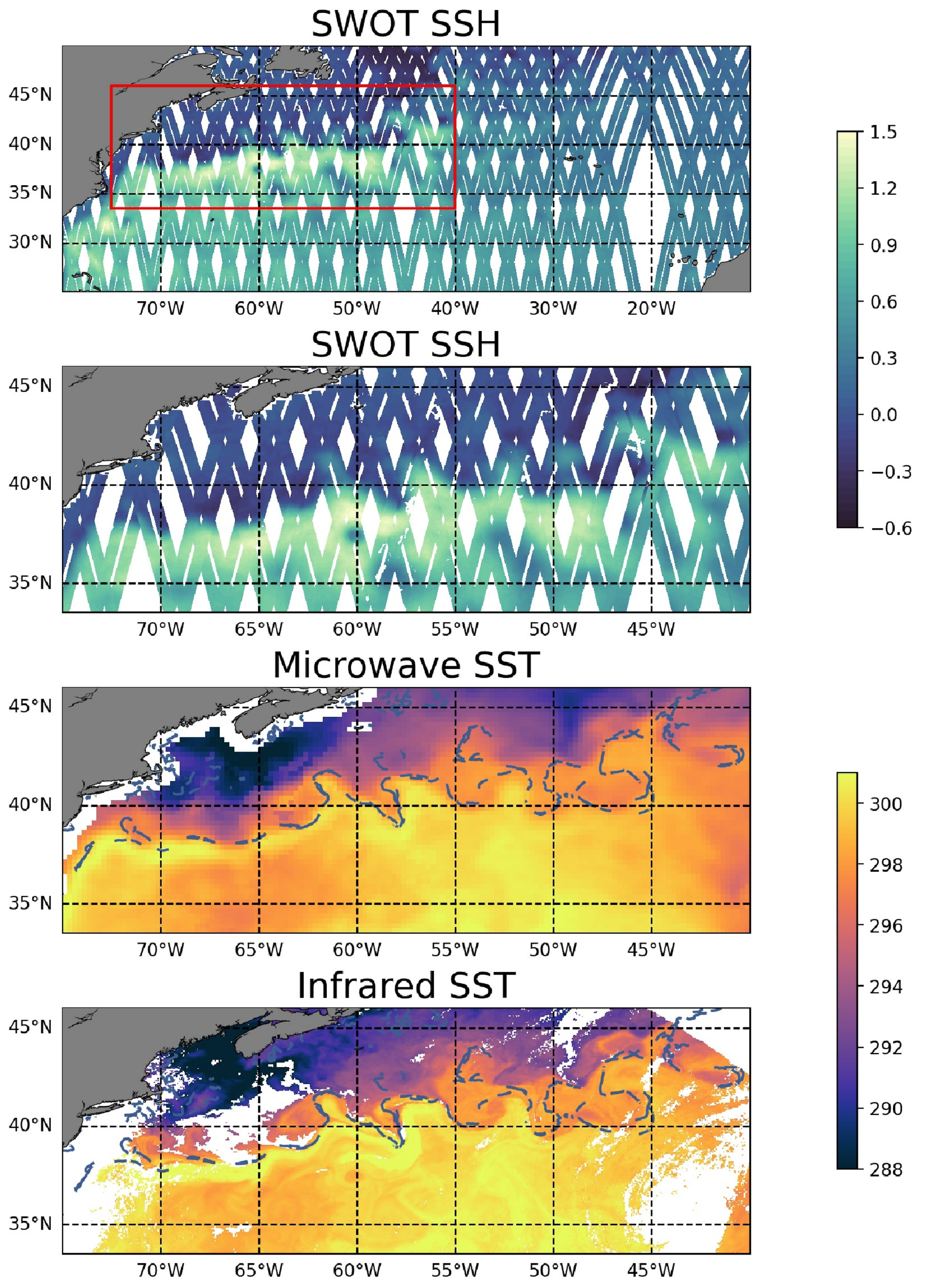

Figure 1. Top: sea surface height (SSH) observed by SWOT over the extended Gulf Stream from 2023-09-13 to 2023-09-23. Bottom: zoom in a small region (65°–55°W, 33°–43°N) to highlight SSH/sea surface temperature (SST) synergies: SSH from SWOT (top), SST map on the 2023-09-15 from the Level-4 Microwave product (middle) and SST map from the Level-3 Geostationary Infrared product (bottom).

Correlations between the two fields thus likely increase at large scales (Tandeo et al., 2014). This is illustrated in Figure 1, i.e., small-scale SST structures observed by SEVIRI geostationary sensor are barely seen by SWOT SSH measurements.

3. Method

3.1. SSH/SST Forward Dynamical Models

Quasi-Geostrophy (QG) models (e.g., Vallis, 2017) offer theoretical robust and practical frameworks to interpret the upper ocean dynamics, down to scales comparable and possibly smaller than the deformation radius. Le Guillou et al. (2023) already considered a 1.5-layer QG model to describe the SSH dynamics. The QG potential vorticity q strictly depends on SSH fields and is conserved along the geostrophic flow $\mathbf{u_g}$, also derived from SSH gradients. The governing equations read:

$$\frac{\partial q}{\partial t} + \mathbf{u_g} \cdot \nabla q = 0 \tag{1a}$$

$$\mathbf{u_g} = \frac{g}{f}\mathbf{k} \times \nabla SSH \tag{1b}$$

$$q = \frac{g}{f}\Delta SSH - \frac{g}{fL_D^2} SSH \tag{1c}$$

where g the gravity constant, f the Coriolis frequency, $\mathbf{k}$ the vertical direction L_D is the Rossby deformation radius, related to the local stratification, Coriolis frequency, and a characteristic vertical length scale. This deformation radius thus explicitly helps define the mesoscale range, over which both kinetic and buoyancy effects are important and strongly interact. Locally and seasonally, such a characteristic length may thus vary.

Combining Equation 1 allows the symbolic formulation of a model for the SSH propagation:

$$SSH_i = \mathcal{M}_{i,i-1}^{SSH}(SSH_{i-1}) + F_i^{SSH} \tag{2}$$

where $\mathcal{M}_{i,i-1}^{SSH}$ is the non-linear QG model operator from time t_{i-1} to t_i and F_i^{SSH} is an extra term to encode processes, for example, ageostrophic motions, not included in the QG setting. Numerically, Equation 2 is integrated as follows. The potential vorticity q_{i-1} is initialized with Equation 1c using SSH data at time t_{i-1}. The geostrophic velocities $\mathbf{u}_{\mathbf{g}_{i-1}}$ are computed using Equation 1b. Then, q_i is computed by integrating Equation 1a in time with a second-order Runge-Kutta scheme. The advection term $\mathbf{u}_{\mathbf{g}_{i-1}} \cdot \nabla q_{i-1}$ is computed with a third-order upwind scheme. Finally, the propagated SSH at time t_i is recovered from q_i through the inversion of the elliptical Equation 1c using a spectral Discrete Sine Transform (DST) solver.

Following Rio and Santoleri (2018), the SST dynamics are approximated by the passive tracer conservation equation:

$$\frac{\partial SST}{\partial t} + \mathbf{u} \cdot \nabla SST = S \tag{3}$$

where $\mathbf{u}$ is the total horizontal surface current vector and S represents the SST source and sink terms (vertical advection, entrainment velocity, diffusion, and atmospheric heat fluxes). Writing $\mathbf{u}$ as the sum of its geostrophic component $(\mathbf{u_g})$ and ageostrophic component $(\mathbf{u_a})$, Equation 3 becomes:

$$\frac{\partial SST}{\partial t} + \left(\frac{g}{f}\mathbf{k} \times \nabla SSH\right) \cdot \nabla SST = S - \mathbf{u_a} \cdot \nabla SST \tag{4}$$

where $\mathbf{u_g}$ has been expressed using Equation 1b. Therefore, we can symbolically write a model for the SST propagation involving SSH:

$$SST_i = \mathcal{M}_{i,i-1}^{SST}(SST_{i-1}, SSH_{i-1}) + F_i^{SST} \tag{5}$$

where $\mathcal{M}_{i,i-1}^{SST}$ is the geostrophic advection model operator from time t_{i-1} to t_i and F_i^{SST} is an extra term which encodes the source and sink terms and the residual horizontal advection by the ageostrophic currents.

To prepare the inversion procedure, SSH and SST fields are gathered in one vector $\mathbf{X} = [SSH, SST]^T$. By combining Equations 2 and 5, we can symbolically write a coupled model for the propagation of SSH and SST variables from time t_{i-1} to t_i, called $\mathcal{M}_{i,i-1}$, function of the unknown catch-all forcing terms vector $\mathbf{F} = \left[F^{SSH}, F^{SST}\right]^T$:

$$\mathbf{X_i} = \begin{bmatrix} SSH_i \\ SST_i \end{bmatrix} = \begin{bmatrix} \mathcal{M}^{SSH}_{i,i-1}(SSH_{i-1}) + F_i^{SSH} \\ \mathcal{M}^{SST}_{i,i-1}(SST_{i-1}, SSH_{i-1}) + F_i^{SST} \end{bmatrix} = \mathcal{M}_{i,i-1}(\mathbf{X_{i-1}}, \mathbf{F_i}) \tag{6}$$

3.2. Variational Inversion

At a specific time t_i, the model state $\mathbf{X_i} = [SSH_i, SST_i]^T$ is given by the knowledge of the initial state $\mathbf{X_0}$ at time t_0 and the time trajectory of the forcing terms $\mathbf{F}$ over the time window $[t_0, t_i]$, called $\mathbf{F_{[0:i]}}$:

$$\mathbf{X_i} = \mathcal{M}_{i,i-1}(\mathbf{X_{i-1}}, \mathbf{F_i}) = \mathcal{M}_{i,0}\left(\mathbf{X_0}, \mathbf{F_{[0:i]}}\right) \tag{7}$$

where $\mathcal{M}_{i,0} = \mathcal{M}_{i,i-1}\mathcal{M}_{i-1,i-2}\dots\mathcal{M}_{1,0}$ is the full forward non-linear coupled model operator from time t_0 to t_i. In the following, the initial state will be prescribed from the operational products described in 2.2, making the model state at time t_i only function of the forcing terms $\mathbf{F}$:

$$\mathbf{X_i} = \mathcal{M}_{i,0}(\mathbf{F}) \tag{8}$$

where we omit the subscript $[0:i]$ of $\mathbf{F}$ for the sake of clarity. Note that in Equation 8, the error in the initial state is neglected.

The resulting inverse problem consists of optimizing the forcing term $\mathbf{F}$ over a specific time window $[t_0, t_1]$ to produce model state trajectories the closest possible to observations $\mathbf{Y^{obs}} = \left[SSH^{obs}, SST^{obs}\right]^T$ while respecting prescribed statistics. This relates to the minimization of the following cost function:

$$J(\mathbf{F}) = \frac{1}{2}\|\mathbf{F} - \mathbf{F^b}\|^2_{\mathbf{B}^{-1}} + \frac{1}{2}\sum_{i=0}^{N_t}\|\mathbf{Y_i^{obs}} - \mathbf{H_i}\mathbf{X_i})\|^2_{\mathbf{R_i}^{-1}} \tag{9}$$

$$= \frac{1}{2}\|\mathbf{F} - \mathbf{F^b}\|^2_{\mathbf{B}^{-1}} + \frac{1}{2}\sum_{i=0}^{N_t}\|\mathbf{Y_i^{obs}} - \mathbf{H_i}\mathcal{M}_{i,0}(\mathbf{F})\|^2_{\mathbf{R_i}^{-1}} \tag{10}$$

where $\|\cdot\|_{\mathbf{W}}$ is the norm induced by a matrix $\mathbf{W}$ and N_t is the number of model time-steps within the time window. Two terms appear in J: (a) a background term measuring the distance from a prior knowledge of $\mathbf{F}$, called $\mathbf{F^b}$, associated with the covariance matrix $\mathbf{B}$; (b) an observation term measuring the distance between the model trajectory, function of the forcing terms $\mathbf{F}$ through Equation 8, and the observations. A specific observation at time $t_i \in [t_0, t_1]$ is associated with a covariance matrix $\mathbf{R_i}$ (representing both observation and model representation errors) and a linear operator $\mathbf{H_i}$, which projects the model state (SSH_i and SST_i) onto the observation coordinates (altimetric 1D tracks for SSH and 2D images for SST).

The minimum of J is found using a descent method that requires the calculation of its gradient with respect to F:

$$\nabla_{\mathbf{F}} J(\mathbf{F}) = \mathbf{B^{-1}}\left(\mathbf{F} - \mathbf{F^b}\right) - \sum_{i=0}^{N_t}\mathbf{M_{i,0}^T}\mathbf{H_i^T}\mathbf{R_i^{-1}}\left(\mathbf{Y_i^{obs}} - \mathbf{H_i}\mathcal{M}_{i,0}(\mathbf{F})\right) \tag{11}$$

where $\mathbf{M_{i,0}^T} = \mathbf{M_{1,2}^T}\mathbf{M_{i,0}^T}\dots\mathbf{M_{i,i-1}^T}$ is the backward integration of the (linear) adjoint model time t_i to t_0.

3.3. Order Reduction

Order reduction is a standard practice in geophysical data assimilation or inversion to overcome the issues of ill-posedness and numerical complexity like in, for example, Robert et al. (2005), for 4Dvar. The inverse problem is solved in spaces with reduced dimensions (one reduced space per variable, SSH or SST). In practice, these spaces are chosen to sufficiently reduce the number of degrees of freedom of the assimilation system while respecting, as much as possible, the spatio-temporal variability of the dynamics. In the present setting, the order reduction is formulated by:

$$\mathbf{F} = \begin{bmatrix} F^{SSH} \\ F^{SST} \end{bmatrix} = \begin{bmatrix} \Gamma^{SSH} & 0 \\ 0 & \Gamma^{SST} \end{bmatrix} \begin{bmatrix} \Phi^{SSH} \\ \Phi^{SST} \end{bmatrix} = \mathbf{\Gamma\Phi} \tag{12}$$

where Γ^{SSH} and Γ^{SST} are mapping operators to map the control vectors in the physical space from their coordinates (Φ^{SSH} and Φ^{SST}) in the reduced spaces. This equation indicates that F^{SSH} and F^{SST} are expressed in reduced bases that are independent of each other. However, SSH dynamics, which are controlled by F^{SSH} through Equation 2, influence the SST dynamics via advection by SSH-derived geostrophic currents, making the inversion of both SSH and SST variables dependent on each other. Thus, although the reduced bases are independent, the assimilation of SSH (SST) impacts the reconstruction of SST (SSH).

The background error covariance matrix **B** plays a central role in optimal estimation, as it represents the uncertainty in the background state. It is used in the cost function to weigh the prior information (the background state) relative to the observations, ensuring that the solution balances the model predictions and the data. The background covariance matrix **B** is then expressed in the reduced space as:

$$\mathbf{B} = \mathbf{\Gamma Q \Gamma^T} \tag{13}$$

where **Q** is the reduced-order background covariance matrix. In this formulation, **B** encapsulates the uncertainty in the control vectors, and the reduced matrix **Q** simplifies the representation of this uncertainty by focusing on the most relevant modes of variability. The reduced-order formulation is advantageous because it reduces the dimensionality of the problem while maintaining the critical spatio-temporal variability needed for accurate assimilation.

A major advantage of order reduction is the ability to choose independent components, resulting in a diagonal **Q** matrix. This simplifies the inversion process, allowing for more efficient computation. The cost function (Equation 9) can then be expressed using the new reduced-order control vector $\mathbf{\Phi}$:

$$J(\mathbf{\Phi}) = \frac{1}{2}\|\mathbf{\Phi} - \mathbf{\Phi^b}\|^2_{\mathbf{Q}^{-1}} + \frac{1}{2}\sum_{i=0}^{N_t}\|\mathbf{Y_i^{obs}} - \mathbf{H_i}\mathcal{M}_{i,0}(\mathbf{\Gamma\Phi})\|^2_{\mathbf{R_i^{-1}}} \tag{14}$$

Similarly, the gradient of J (Equation 11) writes:

$$\nabla_{\mathbf{\Phi}} J(\mathbf{\Phi}) = \mathbf{Q^{-1}}\left(\mathbf{\Phi} - \mathbf{\Phi^b}\right) - \sum_{i=0}^{N_t}\mathbf{\Gamma^T M_{i,0}^T H_i^T R_i^{-1}}\left(\mathbf{Y_i^{obs}} - \mathbf{H_i}\mathcal{M}_{i,0}(\mathbf{\Gamma\Phi})\right) \tag{15}$$

Following Ubelmann et al. (2021), the reduced spaces Γ_{SSH} and Γ_{SST} result from 3-dimensional (space/time) wavelet projections at different spatial scales, temporal extensions, and orientations. Figure 2 shows the space/time structures of several elements centered around the same space-time coordinate. The reader will find the mathematical formulation and all the technical details of the wavelet projections in Ubelmann et al. (2021) (Section 2.3.2.1).

The characteristics of each basis are carefully set to represent the statistics of the unknown forcing terms with a minimum number degree of freedom. For Γ_{SSH}, the basis elements cover wavelengths in the mesoscale range (between 50 and 900 km). A unique temporal extent is associated with each wavelength, evaluated to match the decorrelation time of the SSH DUACS product at that specific wavelength. For instance, 100 km patterns in the main Gulf Stream region have a local time-decorrelation of about 4 days. For Γ_{SST}, the basis elements cover the large mesoscale range (between 300 and 900 km) to limit the projection of the associated forcing fluxes onto the advection scales. F_{SST} likely encodes many processes associated with various time/space scales, and multiple time extents, between 2 and 10 days, are associated with each spatial scale.

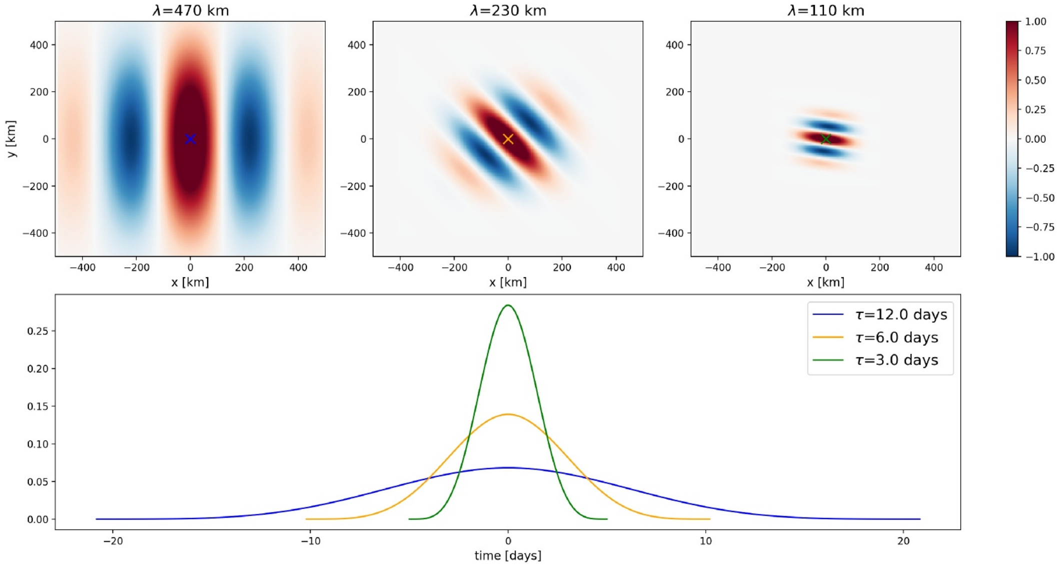

Figure 2. Examples of the space (top) and time (bottom) structures of three basis elements centered around the same space-time coordinate. Here, large spatial scales are associated with long time scales, as it is expected for the sea surface height mesoscale dynamics.

3.4. Numerical Implementation

The experimental space-time domain is divided into overlapping tiles of $10° \times 10°$ in space and 20 days in time. It first allows the parallelization of the minimization procedure to speed up the overall reconstruction. Second, while the spectral solver for the QG elliptic equation requires a constant Rossby deformation radius, the use of tiles allows for consideration of its spatial and temporal variability. In practice, the Rossby deformation radius is estimated by averaging the climatology from Chelton et al. (1998) within each tile.

The forward models, Section 3.1, are implemented using the JAX library to benefit robust automatic differentiation capabilities and seamless GPU acceleration. The model adjoints are automatically computed to calculate the cost function 15. JAX further includes Just-In-Time (JIT) compilation via XLA (Accelerated Linear Algebra), to help compilation of Python functions into optimized machine code, resulting in faster execution times. Furthermore, running the models on a GPU accelerates execution by a factor of 30.

The convergence of the minimization of the cost function (Equation 14) strongly depends on the observational and background statistics, represented by the covariance matrices R and Q. Both matrices are set diagonals, assuming there are no correlated errors in the observations and the basis elements are independent of each other. Observational errors are set to 3 cm for altimeters and 1 K for microwave sensors. As expected, the standard deviation of F_{SSH} is consistent with the spatial power spectrum from altimeter estimates, while the ones of F_{SST} are all set to 1 K/d.

The minimization of the variational cost function is separately performed for each tile using the L-BFGS method. At the start of each minimization procedure, the control vector $\mathbf{\Phi}$ is initialized as the zero vector. The optimized control vector $\mathbf{\Phi}^{\mathbf{opt}}$ is then obtained when the relative variation of the cost function is below 10^{-5}. In practice, fewer than 500 iterations are needed. Reconstructed SSH and SST fields over each tile are computed by integrating Equation 8 using the optimized forcing term $\mathbf{F}^{\mathbf{opt}} = \mathbf{\Gamma\Phi}^{\mathbf{opt}}$ in the physical space. The SSH and SST fields over the full domain are then reconstructed by linearly interpolating the maps of the overlapping tiled areas. The maps are saved every 6 hr at a 10 km resolution.

4. Results

This variational dynamical method, hereafter called VarDyn, is applied to the experimental set-up described in Section 2. In this section, performances of the VarDyn products are assessed against independent data and compared with operational products.

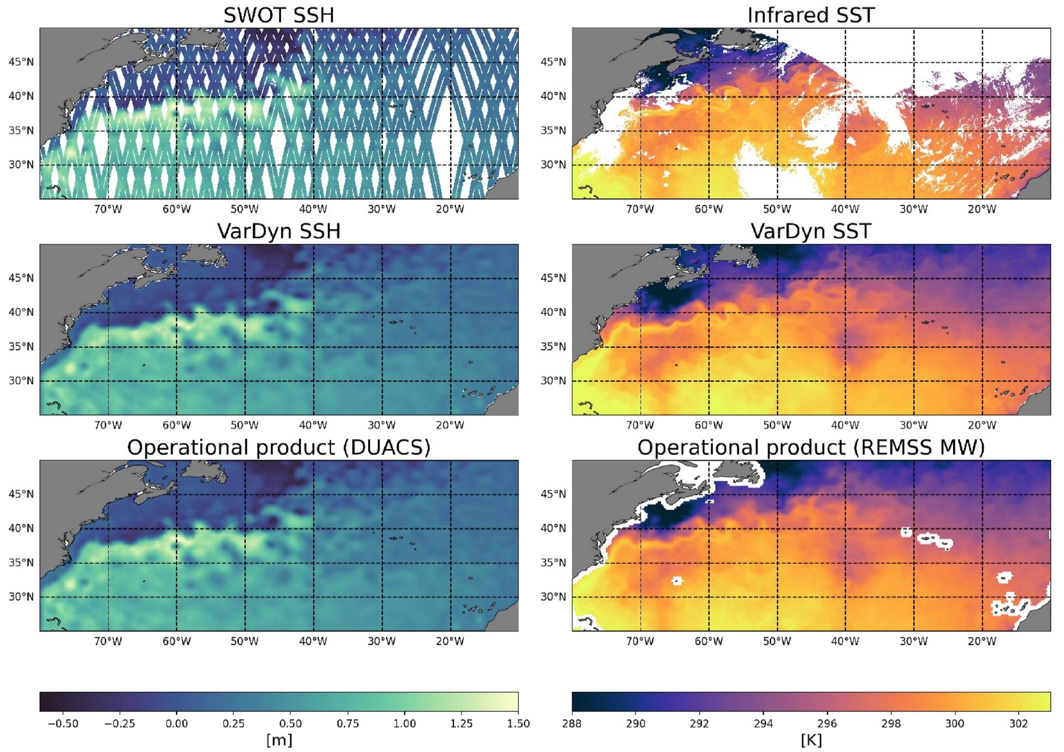

Figure 3. Snapshots of validation data sets (top), VarDyn (middle), and Operational (bottom) products in the study domain on 15 September 2023 for sea surface height (left) and sea surface temperature (right). For SWOT, the data reflected are taken in a 10-day window around the considered date.

Figure 3 illustrates VarDyn SSH and SST maps and operational products, along with independent SWOT SSH and Infrared SST data. Qualitatively, products are similar and appear well correlated to independent data.

Here bellow, in Section 4.1, the validation metrics are presented and later used to analyze the performances in Section 4.2.

4.1. Validation Metrics

The validation metrics are based on statistical and spectral analysis. Both VarDyn and operational products (called x, which refers either to SSH or SST variable) are first projected onto the space/time coordinates of the validation data sets, called x_{true}. Both x and x_{true} are then binned in $1° \times 1°$ boxes over the whole experimental time period to analyze the spatial distribution of the performances.

The first common metric is the Root Mean Square Error (RMSE). For each spatial tile and each variable (SSH or SST), it measures the mean distance between reconstructed and true values:

$$RMSE = \sqrt{\frac{1}{N}\sum_{i=1}^{N_b}(x[i] - x_{true}[i])^2} \tag{16}$$

where N is the number of data points in a tile. The RMSE diagnostics is known to be sensitive to phase error (i.e., the positions of the structures) regardless of their spatial scales. As anticipated, the SST VarDyn product exhibits large-scale bias compared to infrared SST data, strongly affecting the RMSE. This bias largely stems from diurnal variations in the input data sets, filtered out in the operational REMSS gridded product. To best remove this large-scale bias and to focus on the mesoscale dynamics, the RMSE is then evaluated on SST spatial gradients.

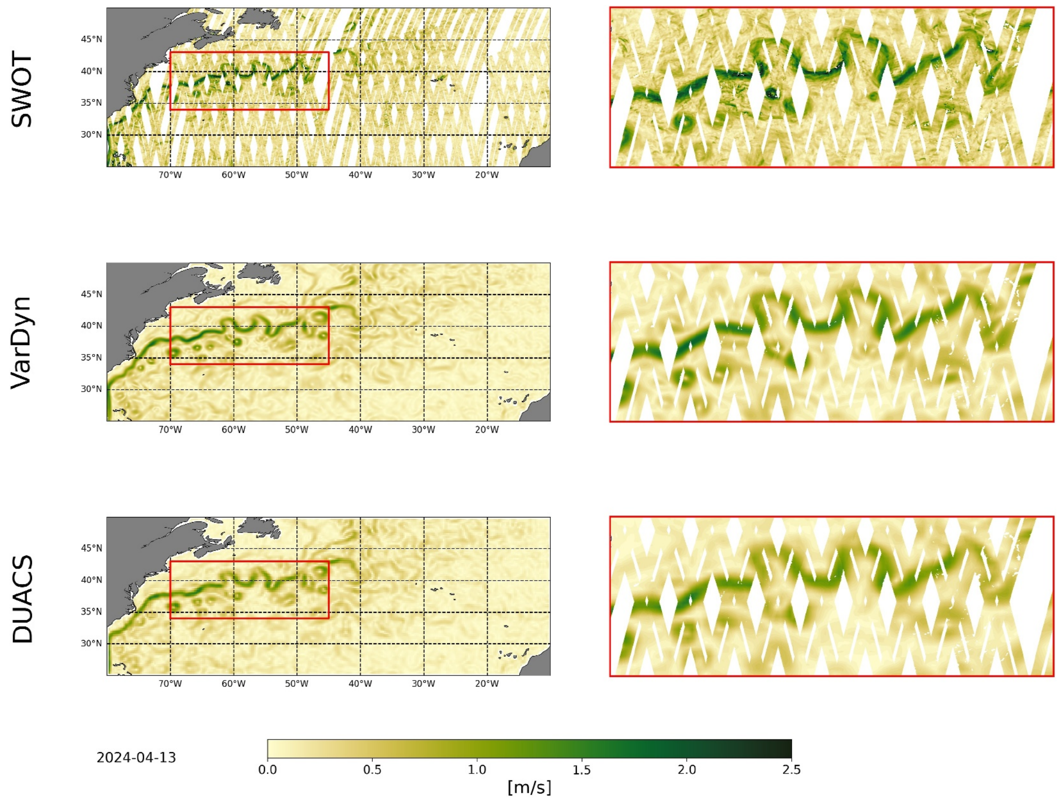

Figure 4. Geostrophic currents for SWOT, VarDyn, and DUACS products on 13 April 2024, over the whole study domain (left) and zoomed in one region along the main current (right).

The second metric is the effective spatial resolution, evaluated from the spatial Power Spectrum Density (PSD). The wavelength criterion λ_{eff} corresponds to the scale below which the PSD of the error $x - x_{true}$ is two times lower than the PSD of the true signal x_{true}:

$$PSD(x - x_{true})[\lambda_{eff}] = \frac{PSD(x_{true})[\lambda_{eff}]}{2} \tag{17}$$

The validation data sets from SWOT and infrared sensors enable 2D PSD computations. For SWOT, the across-track direction is still short compared to the expected resolved scales. λ_{eff} is then calculated for each across-track wavenumber and then averaged by weighting each contribution with the associated PSD for this wavenumber. For infrared SST, the PSD computation is strongly sensitive to data discontinuities, and the cloudy areas are minimized using a 10-day sliding mean. The remaining discontinuities are removed by performing spatial convolutions with the neighboring pixels.

These two metrics, RMSE and effective resolution λ_{eff}, are then evaluated for both VarDyn and operational products. For each metric, the two products are compared by computing the gain or reduction ratio Δ:

$$\Delta M = 100\,\frac{M_{\text{VarDyn}} - M_{Op}}{M_{Op}} \tag{18}$$

where M_{VarDyn} and M_{Op} refer to the value of the metric M (RMSE or λ_{eff}) of the VarDyn and Operational products.

4.2. Performance Analysis

The VarDyn method appears to outperform the DUACS operational system for mapping SSH across the entire study domain. Qualitatively, geostrophic velocities derived from VarDyn SSH fields reveal smaller-scale structures that align better with SWOT estimates (Figure 4). Differences between the VarDyn and DUACS

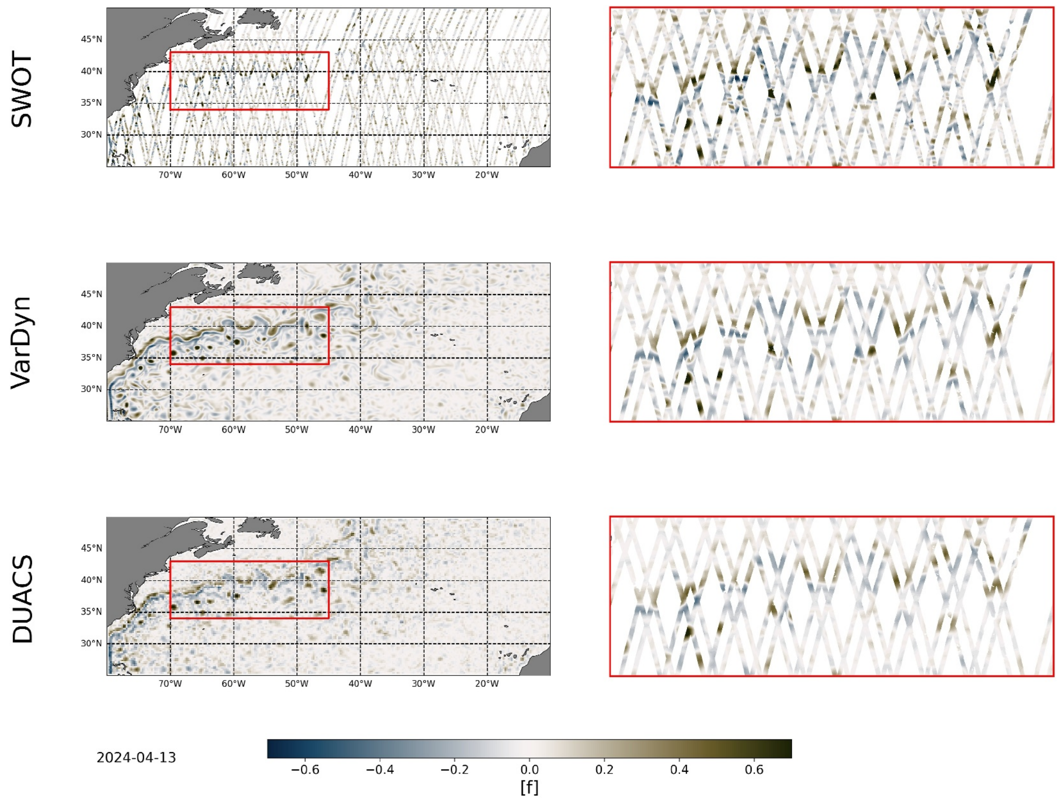

Figure 5. Same as Figure 4 but for the geostrophic relative vorticity derived from sea surface height.

products are even more pronounced in geostrophic relative vorticity fields (Figure 5), where smaller-scale structures are better contrasted, and the continuity of frontal structures and eddies is improved. In this figure, relative vorticity fields from SWOT are derived using a fitting kernel method to mitigate small-scale noise caused by residual instrumental errors and ageostrophic processes. Quantitatively, the VarDyn method demonstrates a clear improvement in RMSE, achieving reductions of 30% in high-energy areas and 10% in low-energy areas (Figure 6). The same trend applies to effective spatial resolutions: most of the improvement occurs in high-energy areas, while VarDyn matches operational resolutions in low-energy areas. Within the main current region (indicated by the green contour in Figure 6), VarDyn SSHs exhibit an average RMSE of 5 cm and an effective resolution of 100 km. These findings confirm that surface geostrophic flow is more strongly constrained by surface buoyancy anomalies in regions characterized by high eddy kinetic energy, strong thermal gradients, and deep mixed layers.

The VarDyn SSH reconstruction particularly benefits from the assimilation of SST when the altimeter constellation is reduced. When only two altimeters are considered, Figure 9 demonstrates that the assimilation of SST significantly reduces the RMSE (by over 20% in high-energy regions) of the SSH reconstruction. For constellations of three or four altimeters, the improvement is smaller but still substantial. However, with more than five altimeters, SST assimilation does not provide significant benefits and can even degrade the RMSE in the northern part of the Gulf Stream extension. This suggests that SSH reconstruction based solely on the QG model is already well constrained with at least five altimeters. Currently (in 2025), seven altimeters are operational. This has not always been the case; for climate studies, the scientific community relies on SSH L4 products derived from a consistent two-altimeter constellation. The VarDyn method offers a robust approach to refine such climate SSH records by jointly assimilating SSH from two altimeters and SST from microwave sensors over the past two decades.

Compared to the REMSS microwave SST products, the VarDyn method ensures better positioning and intensity of high-energy SST fronts. Figure 7 shows that VarDyn SST can depict filaments detected with infrared sensors, which are absent or attenuated in the REMSS products. In terms of quantitative diagnostics (Figure 8), the RMSE

10.1029/2024MS004689

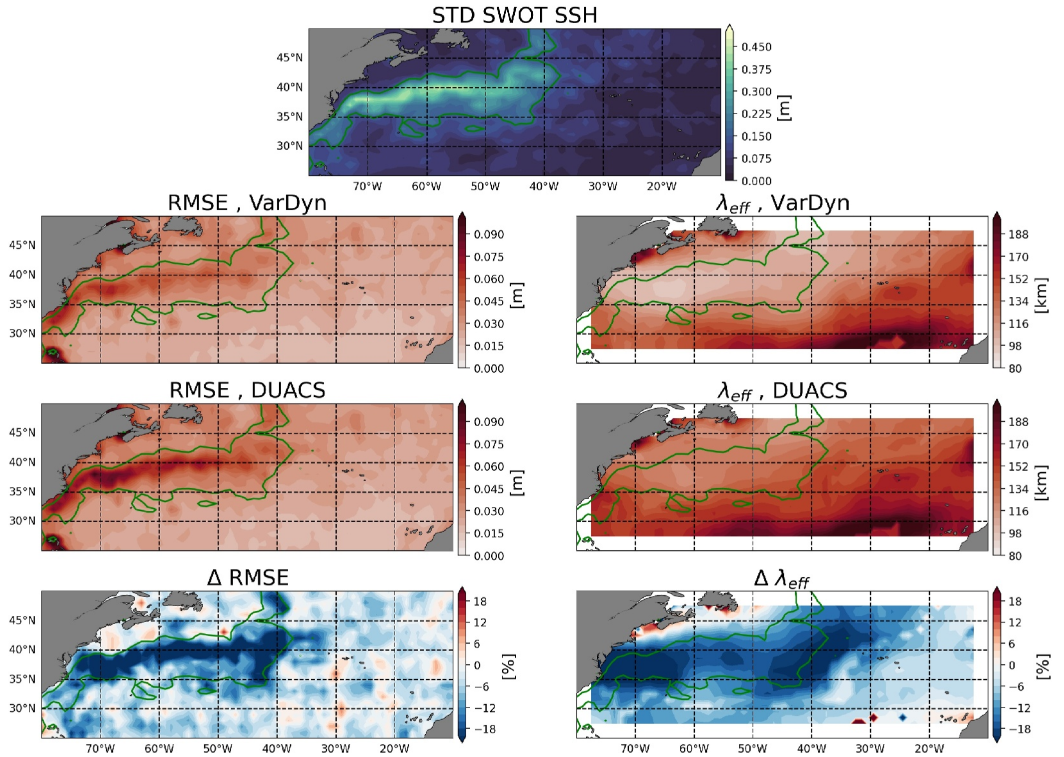

Figure 6. Diagnostics for sea surface height (SSH) reconstruction over the study domain. Top: Standard Deviation (STD) of SSH observed by SWOT. Left: Root Mean Square Error (RMSE) evaluated with SWOT for VarDyn and DUACS products. Right: effective spatial resolution λ_{eff} evaluated with SWOT for VarDyn and DUACS products. The two bottom panels depict the gain/reduction ratio (blue means better performance for VarDyn product relative to the considered metric, RMSE or λ_{eff}). The green line refers to the 0.15 m STD contour.

improves by 5%–10% over the inner domain. However, the RMSE degrades near coastal and open boundary areas. The effective resolution is improved in high-energy areas, as qualitatively illustrated in Figure 7. However, the two metrics disagree in low-energy areas, where RMSE improves while resolution degrades. This discrepancy may arise because the two metrics are computed from different quantities: SST spatial gradients for RMSE (to ignore large-scale biases) and full SST fields for effective resolution.

For future investigations, a unique feature of the VarDyn method is its ability to estimate SST forcing terms. These effective fluxes encompass multiple hidden contributions, including atmospheric fluxes, vertical and ageostrophic advection, and mixed-layer depth variations. For example, Figure 10 illustrates the signature of a hurricane's marine cold wake and the associated SST fluxes derived from VarDyn. Numerous studies have explored the ocean's response to tropical cyclone passages. In their wake, TCs generate a variety of effects that contribute to irreversible vertical mixing through surface stirring, shear at the base of the mixed layer, and convective cooling. This process is typically characterized by the near-instantaneous emergence of a surface cold anomaly, which is sensitive to pre-existing temperature and salinity stratification. The VarDyn approach effectively encodes this localized and instantaneous cooling signature within its residual forcing terms. In the Northern Hemisphere, a pronounced rightward cooling bias often occurs due to the forward motion of TCs. This bias results from resonant coupling between surface winds and clockwise inertial currents, which are accelerated on the right side and decelerated on the left side of the TC's trajectory. Such phenomena are also well captured by the VarDyn residual SST forcing terms. While further investigations are required, VarDyn offers numerous opportunities to study mechanisms such as amplification and restratification rates during extreme events, including cyclones and marine heat waves.

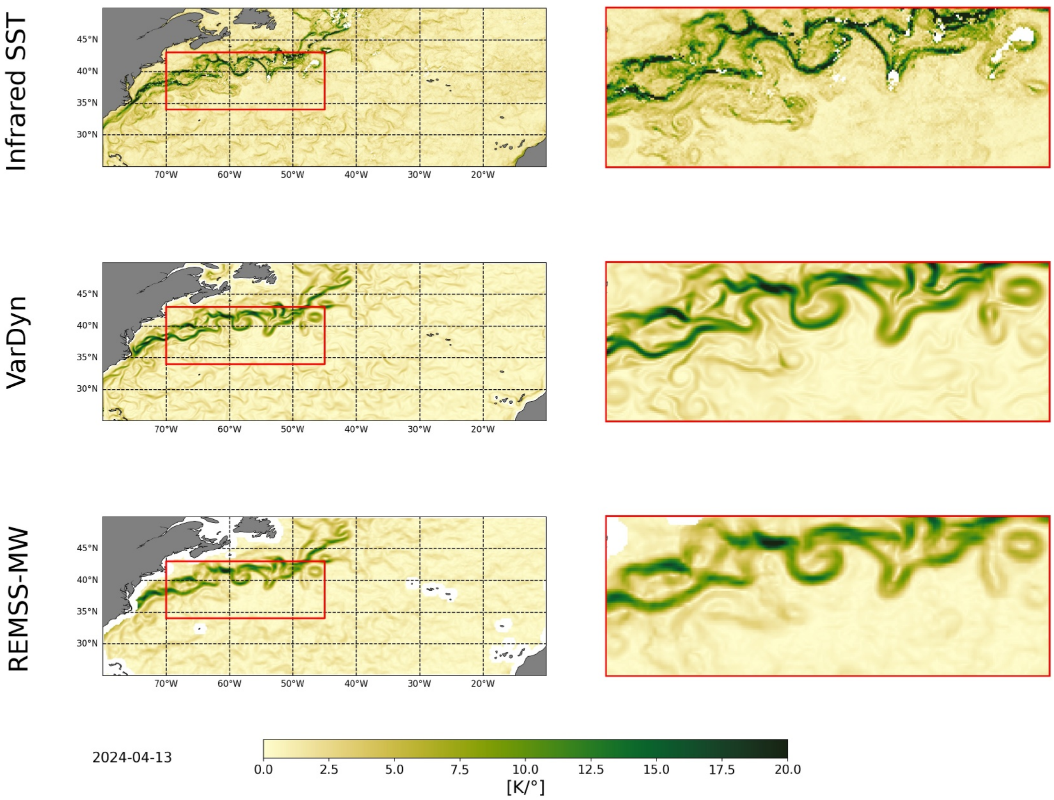

Figure 7. Same as Figure 4 but for spatial gradient of sea surface temperature.

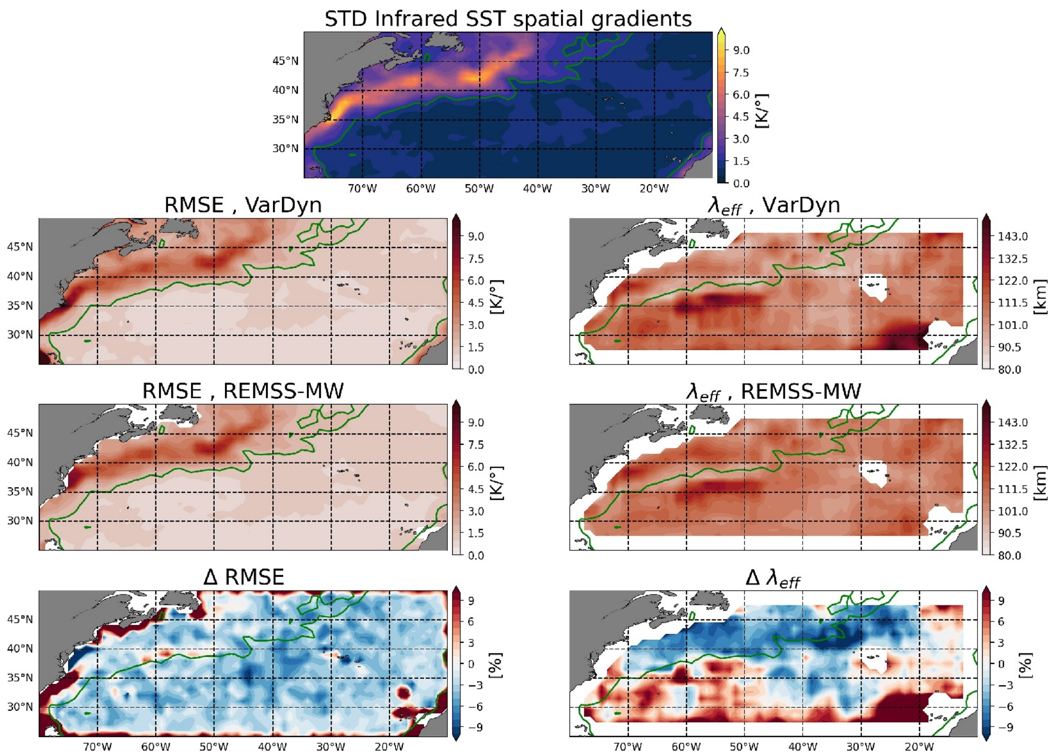

Figure 8. Same as Figure 6 but for sea surface temperature (SST). Note that for SST, the RMSE is computed for spatial gradient to remove large-scale biases. The green line refers to the 1.5 K/° STD contour.

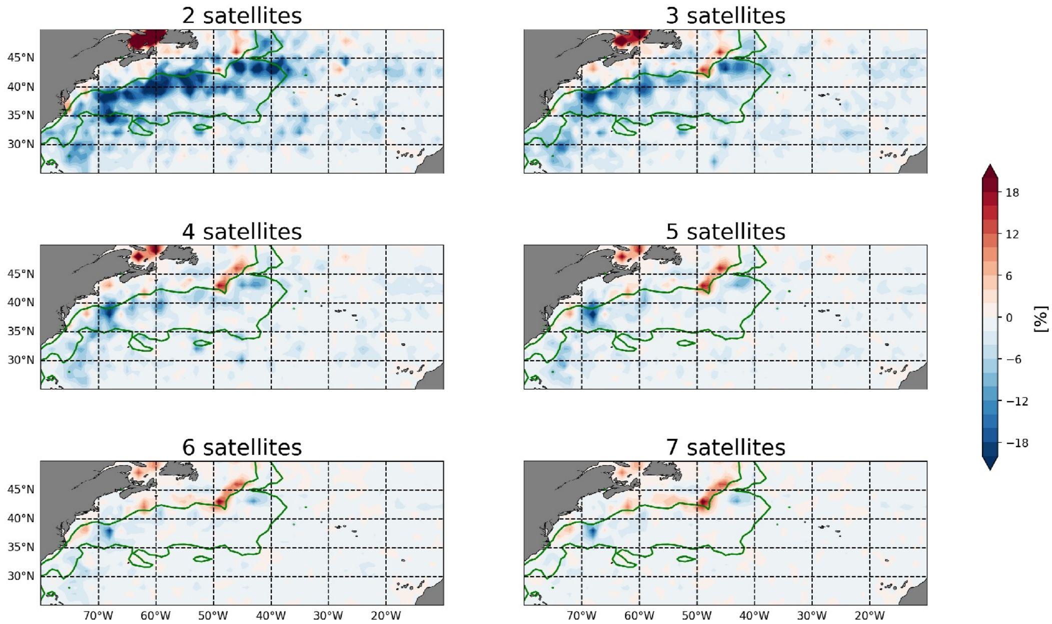

Figure 9. Maps of the RMSE improvement/degradation ratio resulting from jointly considering sea surface temperature for the reconstruction of sea surface height fields, using different satellite constellations composed of 2–7 altimeters. Larger improvements are observed for the 2- and 3-altimeter constellations, especially over the dynamic core region of the Gulf Stream.

5. Conclusions

In this paper, VarDyn is presented to jointly reconstruct SSH and SST fields from partial altimeter and microwave observations. The method strongly inherits from the SSH BFN-QG mapping method (Le Guillou et al., 2023). The algorithm minimizes a variational cost function to constrain the reconstructed SSH and SST trajectories to best fit observations while respecting minimal dynamical principles, here based on QG and passive tracer advection-diffusion models. The minimization is facilitated by expressing the control vector on well chosen reduced basis.

The VarDyn method improves the accuracy of SSH and SST maps compared to operational products, both in terms of RMSE and effective spatial resolution. Most improvements occur in highly energetic regions, mainly along the Gulf Stream and its extension. The VarDyn method is still able to slightly improve the accuracy of SSH maps in low-energetic regions, which is a clear improvement compared to the BFN-QG method. For SST, the

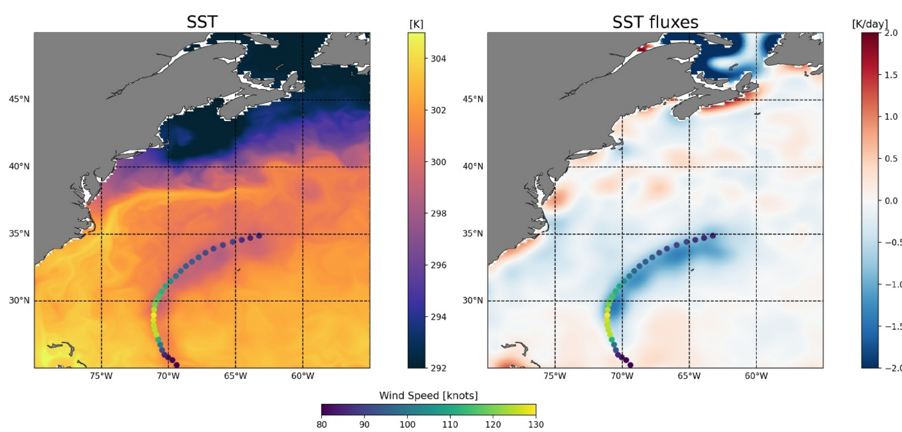

Figure 10. Signature of extra-tropical hurricane Franklin (September 2023) on VarDyn sea surface temperature (left) and the associated estimated fluxes F_{SST} (right).

VarDyn method does not improve the effective spatial resolution in low-energetic regions, which might be due to large-scale biases. Future works should focus on these weaknesses by taking into account diurnal cycle corrections. Still, the generation of a VarDyn climate record of consistent SSH/SST maps, solely based on a 2-altimeter constellation and microwave sensors, can already be performed and is an important perspective.

In this paper, VarDyn has exclusively been applied to the Gulf Stream region, which is characterized by specific and intense dynamical features. Therefore, it does not represent the full spectrum of dynamics observed globally. A step forward in extending the current VarDyn methodology could involve incorporating a physical constraint of higher complexity, such as one based on a Shallow-Water model. This would allow moving beyond the geostrophic assumption by reconstructing unbalanced processes, such as internal tides, which have signatures in altimetry, particularly in SWOT data. Additionally, it would help control the asymmetry of vorticity statistics, where cyclones prevail over anticyclones, and better capture the occurrence of Lagrangian convergence events, such as enhanced tracer gradients. Other strong ageostrophic local motions (e.g., Ekman transport) could also be identified, improving the quality of the reconstructed fields. This approach would also enable extending the SSH/SST reconstructions to the tropical band, an area characterized by strong mesoscale activity. Practically, the transition from QG to Shallow-Water models could be facilitated by using a unified framework, such as the one presented by Thiry et al. (2024).

Another perspective is also to further extend the VarDyn methodology to incorporate the reconstruction of Sea Surface Salinity (SSS) along with SST and SSH. Already evidenced (e.g., Reul et al., 2014), SSS distributions are often largely influenced by upper ocean currents. Especially during summer, when SST and SSH correlations weaken due to extensive heating, SSS can serve as a beneficial complement to SST. However, the coarser resolution of SSS data compared to SST may impact the effectiveness of this approach. Nevertheless, the new ESA CIMR mission (Donlon, 2023) holds strong promise to more consistently constrain reconstructions of high-resolution SSS, SST, and thus SSH data. Including SSS may also be beneficial in consistently extending the QG model to a surface QG (SQG) setting. The SQG model, including next-order ageostrophic corrections and non-uniform stratification distribution, not only presents a simple practical mathematical formulation, but it can better describe smaller-scale generation and dynamics, favoring cyclonic vorticity generation compared to anticyclonic vorticity one.

Finally, the VarDyn methodology provides consistent data-driven estimates, using an optimal blending of observations guided by a minimal physical model. As mentioned above, the combination of SSH and SST is particularly suited for multi-year reconstructions. Long-term consistent reconstructed fields can then provide sufficient means to train Machine-Learning and Deep-Learning methods. Comparable to present-day efforts to robustly emulate weather dynamics, the design of hybrid modeling approaches, based on the combination of a physical core and a deep learning sub-model, may thus be considered. Learning from VarDyn records, an ensemble of short-term upper ocean forecasts may ultimately be obtained, possibly integrating atmosphere ensemble forecasts, to further reconsider assimilation processes to more efficiently integrate observations.

Data Availability Statement

The Level 3 satellite altimetry observations (CMEMS, 2024a) used as input of our method and the operational DUACS Level 4 SSH gridded product (CMEMS, 2024b) used to compare the SSH mapping performances are freely publicly available from the CMEMS data store. The SWOT_L3_LR_SSH product (AVISO/DUACS, 2024), used to validate the SSH mapping performances, is produced and made freely available by AVISO and DUACS teams as part of the DESMOS Science Team project. The Level 3 satellite microwave data from AMSR-2 (Wentz et al., 2021) and GMI (Wentz et al., 2015) used as input of our method are freely publicly available from the REMSS data store. The Level 3 IR data (CMEMS, 2023) used to validate the SST mapping performances are freely publicly available from the CMEMS data store. The operational Level 4 microwave gridded product (Remote Sensing Systems, 2017) used to compare the SST mapping performances is freely publicly available from the NASA Physical Oceanography Distributed Active Archive Center (PODAAC). VarDyn SSH and SST products can be obtained through the ESA Open Science Catalogue for a constellation of two altimeters (Le Guillou et al., 2024a) and seven altimeters (Le Guillou et al., 2024b). The Python code necessary to reproduce the VarDyn products presented in this paper is publicly available in Le Guillou (2024). Finally, the Python code necessary to reproduce the relative vorticity fields from SWOT data is publicly available in Tranchant (2024).

Acknowledgments
We are grateful to the three anonymous reviewers for their detailed and constructive comments that helped us improve our manuscript.

References

Abraham, E. R., & Bowen, M. M. (2002). Chaotic stirring by a mesoscale surface-ocean flow. *Chaos: An Interdisciplinary Journal of Nonlinear Science*, *12*(2), 373–381. https://doi.org/10.1063/1.1481615

Archambault, T., Charantonis, A., Béréziat, D., Mejia, C., & Thiria, S. (2022). Sea surface height super-resolution using high-resolution sea surface temperature with a subpixel convolutional residual network. *Environmental Data Science*, *1*, e26. https://doi.org/10.1017/eds.2022.28

AVISO/DUACS. (2024). SWOT level-3 KaRIn low rate SSH basic (v1.0.2) [Dataset]. *CNES*. https://doi.org/10.24400/527896/A01-2023.017

Ba, S. O., Corpetti, T., Chapron, B., & Fablet, R. (2012). Variational interpolation of multi-modal ocean satellite images. *Traitement du Signal*, *29*(3–5), 433–454.

Ballarotta, M., Ubelmann, C., Pujol, M.-I., Taburet, G., Fournier, F., Legeais, J.-F., et al. (2019). On the resolutions of ocean altimetry maps. *Ocean Science*, *15*(4), 1091–1109. https://doi.org/10.5194/os-15-1091-2019

Ballarotta, M., Ubelmann, C., Rogé, M., Fournier, F., Faugère, Y., Dibarboure, G., et al. (2020). Dynamic mapping of along-track ocean altimetry: Performance from real observations. *Journal of Atmospheric and Oceanic Technology*, *37*(9), 1593–1601. https://doi.org/10.1175/JTECH-D-20-0030.1

Ballarotta, M., Ubelmann, C., Veillard, P., Prandi, P., Etienne, H., Mulet, S., et al. (2023). Improved global sea surface height and current maps from remote sensing and in situ observations. *Earth System Science Data*, *15*(1), 295–315. https://doi.org/10.5194/essd-15-295-2023

Beauchamp, M., Febvre, Q., Georgenthum, H., & Fablet, R. (2023). 4DVarNet-SSH: End-to-end learning of variational interpolation schemes for nadir and wide-swath satellite altimetry. *Geoscientific Model Development*, *16*(8), 2119–2147. https://doi.org/10.5194/gmd-16-2119-2023

Berti, S., & Lapeyre, G. (2014). Lagrangian reconstructions of temperature and velocity in a model of surface ocean turbulence. *Ocean Modelling*, *76*, 59–71. https://doi.org/10.1016/j.ocemod.2014.02.003

Buongiorno Nardelli, B., Cavaliere, D., Charles, E., & Ciani, D. (2022). Super-resolving ocean dynamics from space with computer vision algorithms. *Remote Sensing*, *14*(5), 1159. https://doi.org/10.3390/rs14051159

Chelton, D. B., deSzoeke, R. A., Schlax, M. G., Naggar, K. E., & Siwertz, N. (1998). Geographical variability of the first baroclinic Rossby radius of deformation. *Journal of Physical Oceanography*, *28*(3), 433–460. https://doi.org/10.1175/1520-0485(1998)028⟨0433:GVOTFB⟩2.0.CO;2

Chen, Y., & Yu, L. (2024). Mesoscale meridional heat transport inferred from sea surface observations. *Geophysical Research Letters*, *51*(5), e2023GL106376. https://doi.org/10.1029/2023GL106376

Ciani, D., Rio, M.-H., Menna, M., & Santoleri, R. (2019). A synergetic approach for the space-based sea surface currents retrieval in the Mediterranean Sea. *Remote Sensing*, *11*(11), 1285. https://doi.org/10.3390/rs11111285

CMEMS. (2023). ODYSSEA global ocean - Sea surface temperature multi-sensor L3 observations. [Dataset]. *Copernicus Marine Service*. https://doi.org/10.48670/moi-00164

CMEMS. (2024a). Global ocean along track L3 sea surface heights NRT [Dataset]. *Copernicus Marine Service*. https://doi.org/10.48670/moi-00147

CMEMS. (2024b). Global ocean gridded L4 sea surface heights and derived variables NRT [Dataset]. *Copernicus Marine Service*. https://doi.org/10.48670/moi-00149

Combot, C., Mouche, A., de Boyer Montegut, C., & Chapron, B. (2024). Toward comprehensive understanding of air-sea interactions under tropical cyclones: On the importance of high resolution and multi-modal observations. *Geophysical Research Letters*, *51*(19), e2024GL110637. https://doi.org/10.1029/2024gl110637

Dencausse, G., Morrow, R., Rogé, M., & Fleury, S. (2013). Lateral stirring of large-scale tracer fields by altimetry. *Ocean Dynamics*, *64*(1), 61–78. https://doi.org/10.1007/s10236-013-0671-8

Dibarboure, G., Anadon, C., Briol, F., Cadier, E., Chevrier, R., Delepoulle, A., et al. (2024). Blending 2D topography images from SWOT into the altimeter constellation with the Level-3 multi-mission DUACS system. *EGUsphere*, *2024*, 1–64. https://doi.org/10.5194/egusphere-2024-1501

Donlon, C. (2023). The Copernicus imaging microwave radiometer (CIMR) mission requirements document version 5.0.

Emery, W. J., Thomas, A., Collins, M., Crawford, W. R., & Mackas, D. (1986). An objective method for computing advective surface velocities from sequential infrared satellite images. *Journal of Geophysical Research*, *91*(C11), 12865–12878. https://doi.org/10.1029/jc091ic11p12865

Fablet, R., Chapron, B., Le Sommer, J., & Sévellec, F. (2024). Inversion of sea surface currents from satellite-derived SST-SSH synergies with 4DVarNets. *Journal of Advances in Modeling Earth Systems*, *16*(6), e2023MS003609. https://doi.org/10.1029/2023ms003609

Fablet, R., Febvre, Q., & Chapron, B. (2023). Multimodal 4dvarnets for the reconstruction of sea surface dynamics from SST-SSH synergies. *IEEE Transactions on Geoscience and Remote Sensing*, *61*, 1–14. https://doi.org/10.1109/tgrs.2023.3268006

Flament, P., Armi, L., & Washburn, L. (1985). The evolving structure of an upwelling filament. *Journal of Geophysical Research*, *90*(C6), 11765–11778. https://doi.org/10.1029/jc090ic06p11765

Frenger, I., Münnich, M., Gruber, N., & Knutti, R. (2015). Southern ocean eddy phenomenology. *Journal of Geophysical Research: Oceans*, *120*(11), 7413–7449. https://doi.org/10.1002/2015JC011047

Gaultier, L., Verron, J., Brankart, J.-M., Titaud, O., & Brasseur, P. (2013). On the inversion of submesoscale tracer fields to estimate the surface ocean circulation. *Journal of Marine Systems*, *126*, 33–42. https://doi.org/10.1016/j.jmarsys.2012.02.014

González-Haro, C., & Isern-Fontanet, J. (2014). Global ocean current reconstruction from altimetric and microwave SST measurements. *Journal of Geophysical Research: Oceans*, *119*(6), 3378–3391. https://doi.org/10.1002/2013JC009728

Isern-Fontanet, J., Chapron, B., Lapeyre, G., & Klein, P. (2006). Potential use of microwave sea surface temperatures for the estimation of ocean currents. *Geophysical Research Letters*, *33*(24), L24608. https://doi.org/10.1029/2006gl027801

Isern-Fontanet, J., Shinde, M., & González-Haro, C. (2014). On the transfer function between surface fields and the geostrophic stream function in the Mediterranean Sea. *Journal of Physical Oceanography*, *44*(5), 1406–1423. https://doi.org/10.1175/JPO-D-13-0186.1

Kelly, K. A. (1989). An inverse model for near-surface velocity from infrared images. *Journal of Physical Oceanography*, *19*(12), 1845–1864. https://doi.org/10.1175/1520-0485(1989)019<1845:aimfns>2.0.co;2

Kugusheva, A., Bull, H., Moschos, E., Ioannou, A., Le Vu, B., & Stegner, A. (2024). Ocean satellite data fusion for high-resolution surface current maps. *Remote Sensing*, *16*(7), 1182. https://doi.org/10.3390/rs16071182

LaCasce, J., & Mahadevan, A. (2006). Estimating subsurface horizontal and vertical velocities from sea-surface temperature. *Journal of Marine Research*, *64*(5), 695–721. https://doi.org/10.1357/002224006779367267

Lapeyre, G. (2009). What vertical mode does the altimeter reflect? On the decomposition in baroclinic modes and on a surface-trapped mode. *Journal of Physical Oceanography*, *39*(11), 2857–2874. https://doi.org/10.1175/2009jpo3968.1

Lapeyre, G., & Klein, P. (2006). Dynamics of the upper oceanic layers in terms of surface quasigeostrophy theory. *Journal of Physical Oceanography*, *36*(2), 165–176. https://doi.org/10.1175/jpo2840.1

Le Goff, C., Fablet, R., Tandeo, P., Autret, E., & Chapron, B. (2016). Spatio-temporal decomposition of satellite-derived SST–SSH fields: Links between surface data and ocean interior dynamics in the agulhas region. *Ieee Journal of Selected Topics in Applied Earth Observations and Remote Sensing*, *9*(11), 5106–5112. https://doi.org/10.1109/JSTARS.2016.2605040

Le Guillou, F. (2024). MASSH: MApping SSH python code [Software]. *Github*. Retrieved from https://github.com/leguillf/MASSH

Le Guillou, F., Chapron, B., & Rio, M.-H. (2024a). VarDyn North Atlantic sea surface height and temperature L4 products (Sentinel-3, Sentinel-6, GCOM-W1, GPM) [Dataset]. *ESA Open Science Catalog*. Retrieved from https://opensciencedata.esa.int/stac-browser/#/products/vardyn-ssh-twosat-L4/collection.json

Le Guillou, F., Chapron, R., & Rio, M.-H. (2024b). VarDyn North Atlantic sea surface height and temperature L4 products [Dataset]. *ESA Open Science Catalog*. Retrieved from https://opensciencedata.esa.int/stac-browser/#/products/vardyn-ssh-allsat-L4/collection.json

Le Guillou, F., Gaultier, L., Ballarotta, M., Metref, S., Ubelmann, C., Cosme, E., & Rio, M.-H. (2023). Regional mapping of energetic short mesoscale ocean dynamics from altimetry: Performances from real observations. *Ocean Science*, *19*(5), 1517–1527. https://doi.org/10.5194/os-19-1517-2023

Le Guillou, F., Metref, S., Cosme, E., Ubelmann, C., Ballarotta, M., Sommer, J. L., & Verron, J. (2021). Mapping altimetry in the forthcoming SWOT era by back-and-forth nudging a one-layer quasigeostrophic model. *Journal of Atmospheric and Oceanic Technology*, *38*(4), 697–710. https://doi.org/10.1175/JTECH-D-20-0104.1

Le Traon, P. Y., Nadal, F., & Ducet, N. (1998). An improved mapping method of multisatellite altimeter data. *Journal of Atmospheric and Oceanic Technology*, *15*(2), 522–534. https://doi.org/10.1175/1520-0426(1998)015⟨0522:AIMMOM⟩2.0.CO;2

Liu, Y., Zheng, Q., & Li, X. (2023). Detection and analysis of mesoscale eddies based on deep learning. In X. Li & F. Wang (Eds.), *Artificial intelligence oceanography* (pp. 209–225). Springer Nature Singapore. https://doi.org/10.1007/978-981-19-6375-9_10

Martin, S. A., Manucharyan, G. E., & Klein, P. (2023). Synthesizing sea surface temperature and satellite altimetry observations using deep learning improves the accuracy and resolution of gridded sea surface height anomalies. *Journal of Advances in Modeling Earth Systems*, *15*(5), e2022MS003589. https://doi.org/10.1029/2022MS003589

Mezić, I., Loire, S., Fonoberov, V. A., & Hogan, P. (2010). A new mixing diagnostic and Gulf oil spill movement. *Science*, *330*(6003), 486–489. https://doi.org/10.1126/science.1194607

Oliver, E., Benthuysen, J., Bindoff, N. E. A., Hobday, A. J., Holbrook, N. J., Mundy, C. N., & Perkins-Kirkpatrick, S. E. (2017). The unprecedented 2015/16 Tasman Sea marine heatwave. *Nature Geoscience*, *8*(1), 16101. https://doi.org/10.1038/ncomms16101

Ostrovskii, A., & Piterbarg, L. (1995). Inversion for heat anomaly transport from sea surface temperature time series in the northwest Pacific. *Journal of Geophysical Research*, *100*(C3), 4845–4865. https://doi.org/10.1029/94jc03041

Remote Sensing Systems. (2017). *GHRSST level 4 MW_OI global foundation sea surface temperature analysis version 5.0 from REMSS*. NASA Physical Oceanography Distributed Active Archive Center. https://doi.org/10.5067/GHMWO-4FR05

Resseguier, V., Chapron, B., & Mémin, E. (2022). Effects of smooth divergence-free flows on tracer gradients and spectra: Eulerian prognosis description. *Journal of Physical Oceanography*, *52*(1), 53–74. https://doi.org/10.1175/jpo-d-21-0014.1

Reul, N., Chapron, B., Lee, T., Donlon, C., Boutin, J., & Alory, G. (2014). Sea surface salinity structure of the meandering Gulf Stream revealed by SMOS sensor. *Geophysical Research Letters*, *41*(9), 3141–3148. https://doi.org/10.1002/2014GL059215

Rio, M.-H., & Santoleri, R. (2018). Improved global surface currents from the merging of altimetry and sea surface temperature data. *Remote Sensing of Environment*, *216*, 770–785. https://doi.org/10.1016/j.rse.2018.06.003

Rio, M.-H., Santoleri, R., Bourdalle-Badie, R., Griffa, A., Piterbarg, L., & Taburet, G. (2016). Improving the altimeter-derived surface currents using high-resolution sea surface temperature data: A feasibility study based on model outputs. *Journal of Atmospheric and Oceanic Technology*, *33*(12), 2769–2784. https://doi.org/10.1175/JTECH-D-16-0017.1

Robert, C., Durbiano, S., Blayo, E., Verron, J., Blum, J., & Le Dimet, F.-X. (2005). A reduced-order strategy for 4D-Var data assimilation. *Journal of Marine Systems*, *57*(1), 70–82. https://doi.org/10.1016/j.jmarsys.2005.04.003

Rogé, M., Morrow, R., & Dencausse, G. (2015). Altimetric Lagrangian advection to reconstruct Pacific Ocean fine-scale surface tracer fields. *Ocean Dynamics*, *65*(9–10), 1249–1268. https://doi.org/10.1007/s10236-015-0872-4

Siegelman, L., Klein, P., Rivière, P., Thompson, A. F., Torres, H. S., Flexas, M., & Menemenlis, D. (2020). Enhanced upward heat transport at deep submesoscale ocean fronts. *Nature Geoscience*, *13*(1), 50–55. https://doi.org/10.1038/s41561-019-0489-1

Tandeo, P., Chapron, B., Ba, S., Autret, E., & Fablet, R. (2014). Segmentation of mesoscale ocean surface dynamics using satellite SST and SSH observations. *IEEE Transactions on Geoscience and Remote Sensing*, *52*(7), 4227–4235. https://doi.org/10.1109/TGRS.2013.2280494

Thiry, L., Li, L., Mémin, E., & Roullet, G. (2024). A unified formulation of quasi-geostrophic and shallow water equations via projection. *Journal of Advances in Modeling Earth Systems*, *16*(10), e2024MS004510. https://doi.org/10.1029/2024MS004510

Tranchant, Y.-T. (2024). Geostrophic velocity computation from sea surface height (SSH) data [Software]. *GitHub*. Retrieved from https://github.com/treden/SwotDiag

Tréboutte, A., Carli, E., Ballarotta, M., Carpentier, B., Faugère, Y., & Dibarboure, G. (2023). KaRIn noise reduction using a convolutional neural network for the SWOT ocean products. *Remote Sensing*, *15*(8), 2183. https://doi.org/10.3390/rs15082183

Trott, C. B., Subrahmanyam, B., & Washburn, C. E. (2021). Investigating the response of temperature and salinity in the Agulhas Current region to ENSO events. *Remote Sensing*, *13*(9), 1829. https://doi.org/10.3390/rs13091829

Turiel, A., Isern-Fontanet, J., García-Ladona, E., & Font, J. (2005). Multifractal method for the instantaneous evaluation of the stream function in geophysical flows. *Physical Review Letters*, *95*(10), 104502. https://doi.org/10.1103/PhysRevLett.95.104502

Ubelmann, C., Dibarboure, G., Gaultier, L., Ponte, A., Ardhuin, F., Ballarotta, M., & Faugère, Y. (2021). Reconstructing ocean surface current combining altimetry and future spaceborne Doppler data. *Journal of Geophysical Research: Oceans*, *126*(3), e2020JC016560. https://doi.org/10.1029/2020JC016560

Vallis, G. K. (2017). *Atmospheric and oceanic fluid dynamics*. Cambridge University Press.

Vazquez-Cuervo, J., Font, J., & Martinez-Benjamin, J. J. (1996). Observations on the circulation in the Alboran Sea using ERSI altimetry and sea surface temperature data. *Journal of Physical Oceanography*, *26*(8), 1426–1439. https://doi.org/10.1175/1520-0485(1996)026⟨1426:OOTCIT⟩2.0.CO;2

Vigan, X., Provost, C., & Podesta, G. (2000). Sea surface velocities from sea surface temperature image sequences: 2. Application to the Brazil-Malvinas confluence area. *Journal of Geophysical Research*, *105*(C8), 19515–19534. https://doi.org/10.1029/2000jc900028

Wang, J., Flierl, G. R., LaCasce, J. H., McClean, J. L., & Mahadevan, A. (2013). Reconstructing the ocean's interior from surface data. *Journal of Physical Oceanography*, *43*(8), 1611–1626. https://doi.org/10.1175/JPO-D-12-0204.1

Wentz, F. J., Meissner, T., Gentemann, C., Hilburn, K. A., & Scott, J. (2021). RSS GCOM-W1 AMSR2 daily environmental suite on 0.25 deg grid, version 8.2 [Dataset]. *Remote Sensing Systems*. https://doi.org/10.56236/RSS-bq

Wentz, F. J., Meissner, T., Scott, J., & Hilburn, K. A. (2015). Remote sensing systems GPM GMI (daily) environmental suite on 0.25 deg grid, version 8.2 [Dataset]. *Remote Sensing Systems*. Retrieved from https://www.remss.com/missions/gmi

Zhen, Y., Tandeo, P., Leroux, S., Metref, S., Penduff, T., & Le Sommer, J. (2020). An adaptive optimal interpolation based on analog forecasting: Application to SSH in the Gulf of Mexico. *Journal of Atmospheric and Oceanic Technology*, *37*(9), 1697–1711. https://doi.org/10.1175/JTECH-D-20-0001.1